THE ASTROPHYSICAL JOURNAL, 523:559–565, 1999 October 1

AN *INFRARED SPACE OBSERVATORY* UPPER LIMIT TO THE LOW-MASS STAR HALO IN THE EDGE-ON GALAXY NGC 4565

CHARLES BEICHMAN,[1] GEORGE HELOU, DAVE VAN BUREN, AND KEN GANGA
Infrared Processing and Analysis Center, Jet Propulsion Laboratory, California Institute of Technology, Pasadena, CA

AND

F. X. DESERT
Laboratoire d'Astrophysique de l'Observatoire de Grenoble, France
Received 1998 September 22; accepted 1999 May 14

ABSTRACT

We present deep ISOCAM observations taken at 4.5 μm (LW1) in search of a faint halo surrounding the edge-on spiral galaxy NGC 4565. Such a halo might exist if the massive halo that is needed to explain the flat rotation curve of this galaxy were attributable to a population of faint, red objects. The upper limit, 5.4 kJy sr^{-1} (3 σ) at 20 kpc, reported here excludes a halo consisting of late-M dwarfs distributed in a spherical halo but not of lower luminosity brown dwarf stars.

Subject headings: galaxies: halos — galaxies: individual (NGC 4565) — galaxies: stellar content — infrared: galaxies

1. INTRODUCTION

The dynamics of stars, galaxies, and clusters of galaxies offer strong circumstantial evidence for the existence of substantial amounts of matter that exerts a gravitational influence but that is not apparent at visible wavelengths. Progress has been made in identifying the nature of the halo material. The direct detection of dark matter in the halo of the Milky Way (Alcock et al. 1997a) through gravitational microlensing suggests that the halo population of our galaxy might consist of low-mass stars, possibly white dwarf stars. Sackett et al. (1994) detected faint light in a halo around NGC 5907 on a scale large enough to account for the flat rotation curve seen in that galaxy. The colors of that faint halo (Rudy et al. 1997) are consistent with a mixed population of very red stars.

But direct results on galactic halos are few, and arguments continue about the nature of the dark matter. A possible refuge for baryonic dark matter is faint red stars at or below the low-mass cutoff of the main sequence. A cloud of brown dwarfs could have escaped detection at visible wavelengths but could account for the missing halo matter if present in sufficient number. As described below, simple models of a red star or brown dwarf halo suggest a 4.5 μm halo brightness of 0.2–10 kJy sr^{-1} for the $\sim 3.5 \times 10^{11}\ M_\odot$ halo needed to account for the rotation curve of NGC 4565.

2. OBSERVATIONS

2.1. *Observing Strategy*

2.1.1. *Choice of Galaxy*

We selected the edge-on galaxy NGC 4565 (Table 1) out of an extensive list of edge-on galaxies available in the NASA Extragalactic Database. Selection criteria included high ecliptic and galactic latitudes and low 60 and 100 μm cirrus on the *IRAS* images. The galaxy NGC 5907 also met these criteria but was observed as part of the *Infrared Space Observatory* (*ISO*) guaranteed time for this same scientific goal. NGC 4565 has a flat rotation curve (Casterno & Van Gorkom 1991; Rupen 1991) extending over 30 kpc with an inferred total mass of dark matter of $3.5 \times 10^{11}\ M_\odot$ (see below). The normal constituents of the galaxy appear to be well confined to a narrow disk, with little extraplanar emission, other than a well-defined bulge, seen at optical (Rand et al. 1992), near-IR (Rice et al. 1996), and radio (Rupen 1991) wavelengths or in X-rays (Vogler, Pitesch, & Kahabka 1996).

2.1.2. *Choice of Observational Parameters*

The expected halo signal is small (≤ 1 kJy sr^{-1}) compared with the zodiacal, Milky Way, and host galactic foregrounds. We elected to observe using ISOCAM with the CAM03 beam switch macro in the 4.5 μm (LW1) filter. This wavelength maximizes the contrast of the halo with respect to the zodiacal emission for star/brown dwarf masses in the range 0.02–0.2 $M_\odot$. In the LW1 filter the halo emission could be as bright as 0.1% of the zodiacal emission. At longer wavelengths, the contrast with respect to the zodiacal emission is 2 orders of magnitude worse, making the experiment difficult for an observatory embedded within the local zodiacal cloud.

An additional motivation for selecting the LW1 filter is avoidance of galactic cirrus. There is a minimum in the emission from small particles in the 4.5 μm window, while the LW2 filter contains a number of polycyclic aromatic hydrocarbon features (Bernard et al. 1994) that could introduce spurious Milky Way emission into the observations. The estimated cirrus brightness at 4.5 μm is $(4 \times 10^{-4}) I_\nu(100\ \mu\text{m})$ MJy sr^{-1}, where $I_\nu(100\ \mu\text{m})$ is the *IRAS* 100 μm intensity. In regions of weak *IRAS* cirrus, $I_\nu(100\ \mu\text{m}) \sim 1$ MJy sr^{-1}, the cirrus intensity at 4.5 μm should be less than 0.4 kJy sr^{-1}, with gradients across the observed region being smaller still.

Observations were made using 6″ pixels as a compromise between large field of view (180″), sensitivity to low surface brightness, and good camera operation. The best possible photon noise-limited sensitivity expected for the observational procedure outlined below after averaging over all pixels in the array is approximately 1 $\sigma = 0.2$ kJy sr^{-1}. The final sensitivity of these observations is approximately 2–3 kJy sr^{-1} (1 σ), less than optimum because of low-level drifts in detector gain and dark current due to effects of changing illumination and charged particle events.

[1] chas@ipac.caltech.edu.

TABLE 1

PROPERTIES OF NGC 4565

Parameter	Value
α (1950)	$12^h33^m52^s$
δ (1950)	26°15′47″
Orientation angle	136° (east of north)
Galactic latitude	86°
Ecliptic latitude	27°
Distance	10.0 Mpc[a]
Size (B = 25 mag s^{-2})	15.′9 × 1.′85
	49 kpc × 5.7 kpc
Integrated V brightness	10.4 mag
Sampling along minor axis	±4′, 6.′8 (10′ south and 17.′2′north) ±12, 20 (30 south and 50 north) kpc

[a] Distance estimates range from 9.7 to 10.3 Mpc (Simard & Pritchet 1994). We adopt 10 Mpc.

2.1.3. *Observational Sequence*

The observational sequence was designed to minimize instrumental drifts and to provide spatial and temporal chopping on as many scales as possible (Fig. 1). An observational sequence, denoted here as a "scan," consisted of 550 s of array stabilization followed by concatenated ON-OFF pairs made at six positions along the minor axis of the galaxy. The observation at each minor axis position consisted of 16 10 s integrations at (1) the ON position; (2) at the OFF_E position displaced 40′ to the east in ecliptic coordinates; (3) at the ON position again; and (4) at the OFF_W position displaced 40′ to the east in ecliptic coordinates. The OFFs were displaced in ecliptic longitude relative to the ON position to provide a direct monitor of the instrumental stability using the gradient in the zodiacal emission. No observation was made of NGC 4565 itself to avoid imprinting light from the galaxy onto the ISOCAM array. Filter changes were suppressed during the entire sequence of observations to minimize flux-induced responsivity changes.

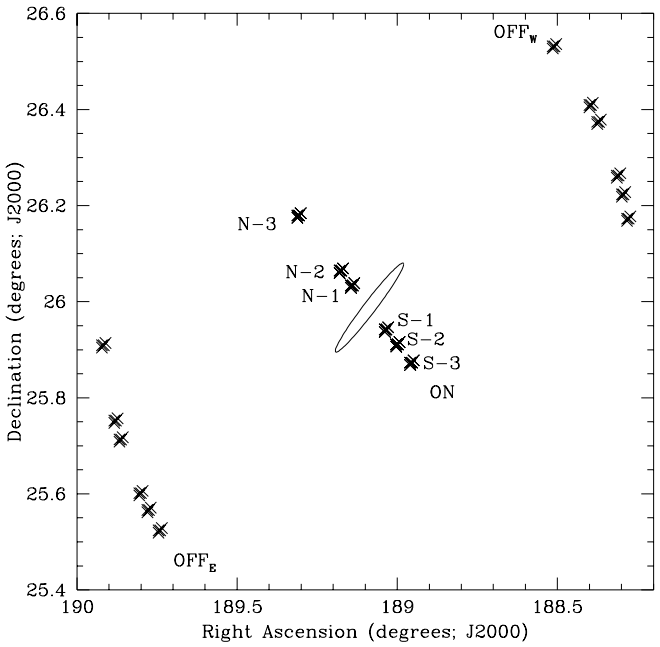

FIG. 1.—Schematic map of the region around NGC 4565 showing the positions on the ON and OFF points. The galaxy is denoted by the blue light B_{25} contour at 25 mag arcsec^{-2} (Table 1).

The scans along the minor axis of the galaxy were repeated on four separate occasions, denoted as scans 1, 2, 3, and 4. Small, ∼15″, offsets were applied to the nominal positions to impose a dithering pattern designed to improve the flat-fielding and bad pixel rejection. To mitigate against direction-dependent effects in the data or data reduction, two scans were made with the telescope stepping northeast and two stepping southwest. Because of observing time constraints, two positions were observed only 3 instead of 4 times. Figure 1 and Table 2 summarize the scan strategy and the *ISO* observing log. The total integration time for those fields observed all 4 times was about 640 s.

2.2. *Data Reduction*

The data for each position within each scan were calibrated using library flat and dark frames and nominal sensitivity values. Automatic deglitching was done using a multiresolution median filtering method (Starck et al. 1998). Further hand deglitching removed data from pixels whose responsivity or offset level was obviously affected by cosmic-ray hits. The calibrated median of all remaining pixels is shown in Figure 2 for each position within scans 1–4. The surface brightness emission is close to that predicted by model for the zodiacal light (Good 1994; Reach et al. 1995), i.e., 200 kJy sr^{-1}. However, the signals at the first position in each scan fall systematically above the remaining values in the scan sequence. Additionally, the signal level seen in the data for the first position (ON_1, OFF_E, ON_2, OFF_W) declines with time. We conclude that there is a residual transient response even after the 550 s of stabilization. Examination of the difference between the first and second ON observation at each position, ON_1-ON_2 (Fig. 3), confirms that the array has not stabilized during the first set of integration.

The difference OFF_E-OFF_W measures the zodiacal light gradient due to a change of about ±40′ in ecliptic latitude (more accurately, cone angle with respect to the Sun at the epoch of observation). The median value of the OFF_E-OFF_W differences are shown for scans 1–4 in Figure 4. The predicted level of the change, −3.5 kJy sr^{-1} on day 184, is consistent with the measurements -5.1 ± 1.7 kJy sr^{-1}. The -4.9 ± 0.9 kJy sr^{-1} measured on day 221 is about a factor of 2 lower than the predicted value of −9 kJy sr^{-1}. The agreement, while not perfect, is encouraging given the uncertainties in the model as well as various calibration effects. The uncertainties in the measurements in the zodiacal gradient serves as a valuable indicator of the uncertainties expected for the halo emission from NGC 4565.

TABLE 2

ISO Observing Log

B (1950)	*ISO* Observation[a]	Direction	*B* (1950)	Observation[a]	Direction
Position: South-3; Scans: 1, 2, 3, 4			Position: North-1; Scans: 1, 2, 3, 4		
$12^h33^m20^s.2$, 26°08′54″, 30 kpc south, on minor axis.....	18401807[b]	North going	$12^h34^m04^s.7$, 26°18′32″, 12 kpc north, on minor axis.....	18401810	North going
	22100524	South going		22100521	South going
	22100618	South going		22100615	South going
	22100701[b]	North going		22100704	North going
Position: South-2; Scans: 1, 2, 3, 4			Position: North-2; Scans: 2, 3, 4		
$12^h33^m30^s.8$, 26°11′11″, 20 kpc south, on minor axis.....	18401808	North going	$12^h34^m13^s.2$, 26°20′23″, 20 kpc north, on minor axis.....	18401811	North going
	22100523	South going		22100520	South going
	22100617	South going		22100614	South going
	22100702	North going		Not observed	...
Position: South-1; Scans: 1, 2, 3, 4			Position: North-3; Scans: 2, 3, 4		
$12^h33^m39^s.3$, 26°13′02″, 12 kpc south, on minor axis.....	18401809	North going	$12^h34^m45^s.0$, 26°27′16″, 50 kpc north, on minor axis.....	18401812	North going
	22100522	South going		22100519[b]	South going
	22100616	South going		22100613[b]	South going
	22100703	North going		Not observed	...

[a] CISP numbers include day number and a sequence number. Day 184 corresponds to 1999 May 19; day 221 corresponds to 1996 June 25.

[b] Rejected because of residual transient response.

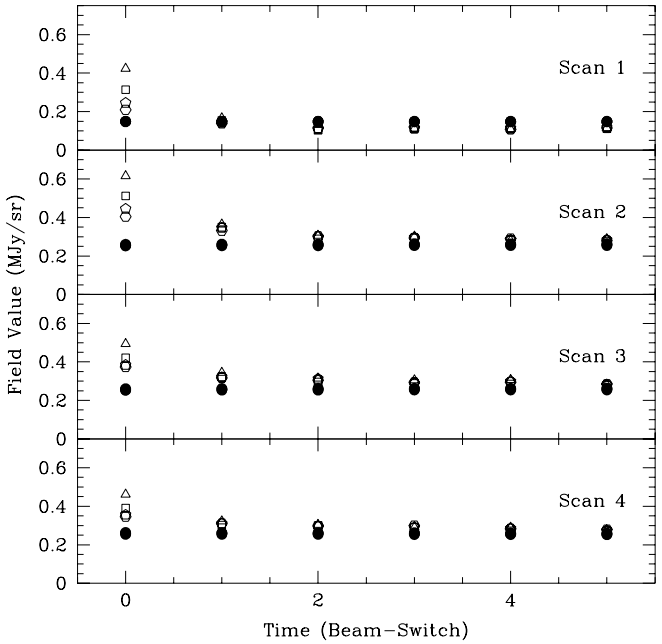

FIG. 2.—Median values of the fields as measured in each scan are presented in time order, from one beam switch position to the next. Triangles correspond to the first ON position, squares to the first OFF field, pentagons to the second ON position, and hexagons to the second OFF position. Solid points correspond to the expected values according to a model for zodiacal thermal emission (Good 1994). Note that the sky position corresponding to a datum within each scan depends on the direction of the scan (Table 2).

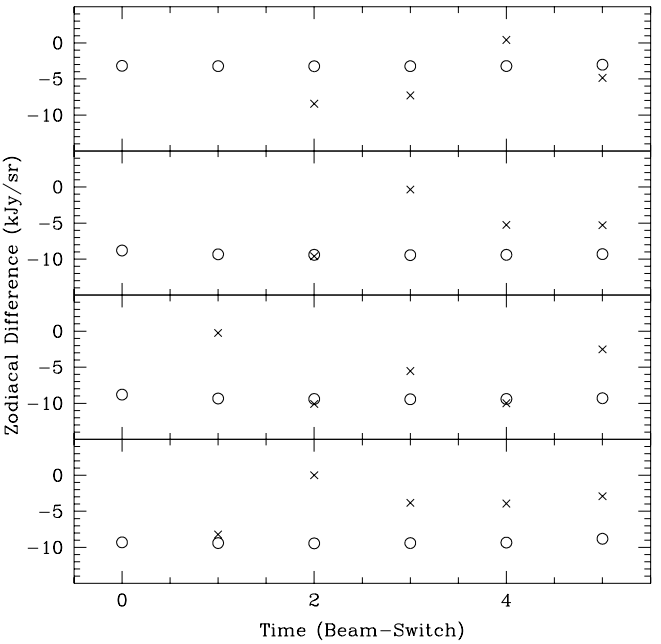

FIG. 4.—Difference between the two OFF positions at a given scan position is a measure of the difference in the brightness of the zodiacal light as a function of ecliptic longitude. The four panels give the data (*crosses*) and zodiacal model predictions (*circles*) for the four scans, presented in time order.

We next formed the beam switch differences needed to measure the halo of NGC 4565. We took two types of difference to monitor systematic effects: (1) to exclude possible transient effects in the first ON position, we calculated ON_2 minus the average of the two OFFs (Fig. 5, *crosses*); (2) to obtain the theoretically best possible signal-to-noise ratio, we calculated the average of the two ONs minus the average of the two OFFs (*squares*). The scan-by-scan data are shown in Figure 5.

Finally, we combined data for each sky position observed within the four scans. Since we ignored the first measurement in each set of observations to minimize residual transients, there are only two measurements at the two positions

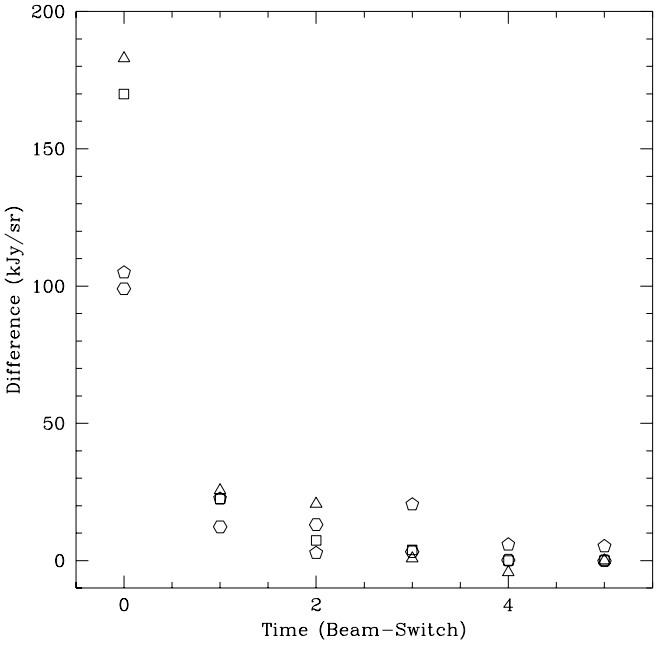

FIG. 3.—Difference between first and last observation at the ON position for each point in the scans are presented in time order. The initial strength of the ISOCAM transient decay is obvious from the signal seen between the two ON observations at the first scan position. Scans 1–4 are encoded using triangles, squares, pentagons, and hexagons, respectively.

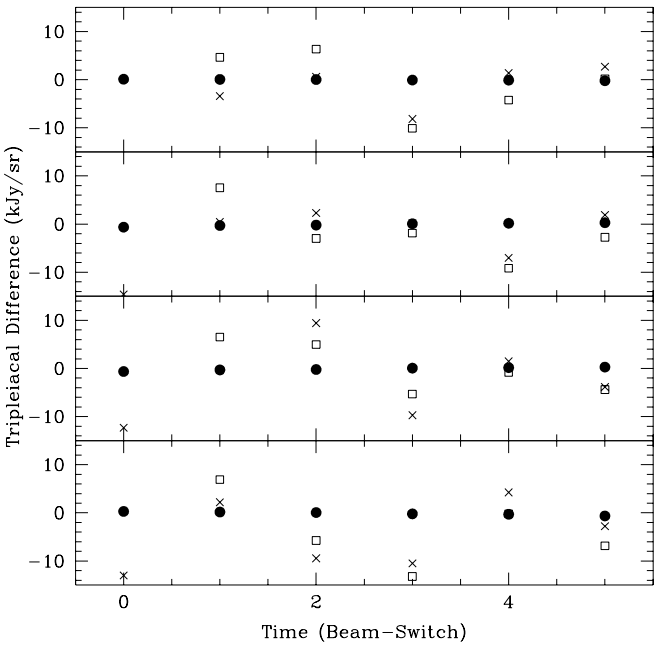

FIG. 5.—Triple differences for data along each scan presented in time order. Symbols denote second ON minus average of two OFFs (*crosses*) or average of two ONs minus average of two OFFs (*squares*).

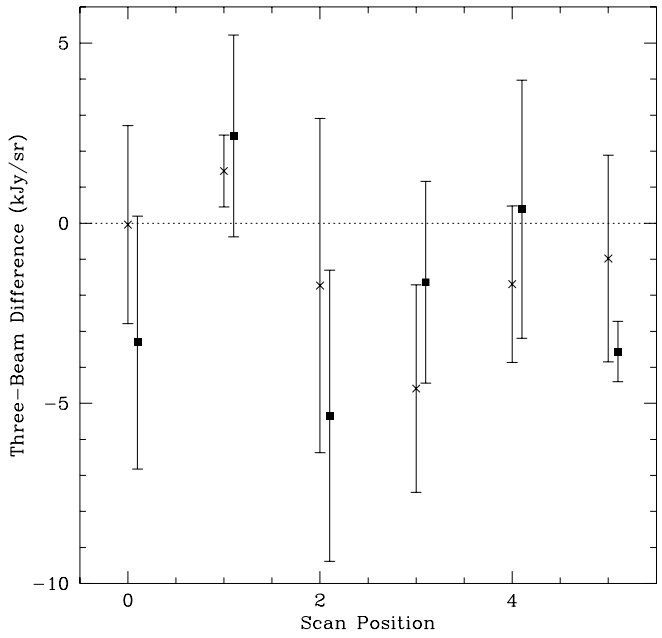

FIG. 6.—Triple differences shown in the previous figure give the best estimates of the halo brightness at the positions sampled. The x-axis denotes position along the scan, taking into account scan direction. The data points extend from the south-3 position on the left to the north-3 position on the right. Crosses correspond to first form of beam switch difference, squares to the second. Error bars are 1 σ. The points are offset from each other for clarity.

farthest north and south of the galaxy. For each position we formed the average and sigma of the two or four measurements using both forms of the differences shown in Figure 5. The final results are shown in Figure 6. The more conservative measurement (difference type 1, above) is summarized in Table 3 and includes the σ-weighted average of the north and south points at 12 and 20 kpc from the galaxy. There is no increase in signal as one moves closer to the galaxy along the minor axis. The 3 σ limit to the brightness of the galaxy halo 20 kpc away from the center is 5.4 kJy sr^{-1}. The 4.5 μm NITE rocket observations of NGC 4565 (Uemizu et al. 1998) detected the starlight from the galaxy and set limits comparable to those reported here for the halo, $\sim$4.5 kJy sr^{-1} (3 σ). The sensitivity of our *ISO* measurements is comparable to *ISO* limits on the halos of other galaxies (Gilmore & Unavane 1998).

3. DISCUSSION

What little is known about galaxy halos has been determined from dynamical clues (Trimble 1987; Ashman 1992):

TABLE 3

MEASUREMENTS OF NGC 4565 HALO

Position	Median Surface Brightness (kJy sr^{-1})
South-3	-0.0 ± 2.8
South-2	1.2 ± 1.0
South-1	-1.8 ± 4.6
North-1	-4.8 ± 2.9
North-2	-1.8 ± 2.2
North-3	-1.0 ± 2.9
Average (north + south)-1[1]	-4.0 ± 2.5
Average (north + south)-2[1]	0.7 ± 1.8

[1] The σ-weighted average of north and south points.

a scale length between 1 and 10 kpc with a maximum extent of 25–50 kpc and a total dark mass ranging from $10^7\ M_\odot$ in dwarf irregular galaxies to $10^{12}\ M_\odot$ in galaxies like the Milky Way. We know little about the halo content even if it is baryonic. Analyses of Large Magellanic Cloud microlensing amplitude variations (Alcock et al. 1993, 1997a; Aubourg et al. 1993) suggest objects with masses of a few 0.1 $M_\odot$ (Alcock et al. 1997a). The detections of a halo in R band around NGC 5907 (Sackett et al. 1994) and at V, I, and B bands (Lequeux et al. 1996, 1998) suggest a halo of very late, possibly metal-rich, M stars (Lequeux et al. 1998). Rudy et al. (1997) have also measured the NGC 5907 halo at J and K in the near-infrared and found that a peculiar mixture of stellar types is required to fit the colors of the halo.

If red stars or substellar objects (brown dwarfs) are responsible for the halo, then their emission should be prominent in the infrared, at wavelengths that range from 1 to 60 μm depending on the mass, age, temperature, and chemical composition (Stevenson 1991; Burrows et al. 1997). As mentioned below, the presence of molecular bands can seriously affect the detectability of these objects, particularly in the 1–2 μm region. We predict the brightness of the halo emission as follows. Let the density distribution of the halo follow that expected for an isothermal sphere with core radius, $R_{\rm core}$ (Bahcall & Soneira 1980; Kent 1986):

$$\rho(r) = \frac{\rho_0}{1 + (r^2/R_{\rm core}^2)}\,, \tag{1}$$

where $\rho_0 = V_{\rm max}^2/2\pi G R_{\rm core}^2$ and $V_{\rm max}$ is the maximum velocity of the galaxy rotation curve. Then the total mass in a halo extending to a maximum radius, $R_{\rm max}$, is given by

$$M_{\rm Tot} = 4\pi\rho_0 R_{\rm core}^3 \left(\frac{R_{\rm max}}{R_{\rm core}} - \tan^{-1}\frac{R_{\rm max}}{R_{\rm core}}\right). \tag{2}$$

The surface brightness of the halo at a given impact parameter, $\beta R_{\rm max}$, is given by

$$I_\nu(\beta) = \pi a^2 B_\nu(T) N(\beta)\,, \tag{3}$$

where $N(\beta)$ is the column density of objects assumed to be emitting as blackbodies of radius a. While the spectra of M stars and brown dwarf stars deviate *strongly* (factors of $\sim$10!) from that of a blackbody at wavelengths around 1–2 μm because of molecular absorption by methane and other species (Marley et al. 1997; Geballe et al. 1996), the blackbody approximation is less in error at the longer wavelengths considered here. For example, Figures 12–14 of Burrows et al. (1997) show that the 4–5 μm spectrum is relatively free of absorption. Furthermore, there is considerable evidence that the deviations from blackbody emission may be considerably less than predicted from atmospheric models because of the effects of dust (Leggett et al. 1998). The blackbody assumption made here is probably in error by no more than a factor of 2 at 4.5 μm (cf. models presented by Saumon et al. 1994). The models for luminosity and temperature as a function of time adopted here (Burrows et al. 1997) are for solar-metallicity objects. Obviously, a putative population of halo objects could have metallicity far lower than solar. Models for stars at the hydrogen-burning limit (Chabrier & Baraffe 1997) show a factor of 2 range in the predicted 4.5 μm *blackbody* emission for metallicities varying from [M/H] = -2 to 0.

The column density at impact parameter $\beta R_{\rm max}$, $N(\beta)$, is given by

$$N(\beta) = 2n_0 \beta R_{\rm max} \int_0^{\theta_{\rm max}} \frac{1}{\gamma^2 + \cos^2\theta} = \frac{2n_0 R_{\rm core}}{\sqrt{(1+\gamma^2)}} \tan^{-1}\left[\frac{R_{\rm max}}{R_{\rm core}} \frac{\sqrt{(1-\beta^2)}}{\sqrt{(1+\gamma^2)}}\right], \quad (4)$$

where $\gamma = \beta R_{\rm max}/R_{\rm core}$ and $\theta_{\rm max} = \cos^{-1}\beta$. For a population of objects with a single mass, m_*, the central number density of objects, is $n_0 = \rho_0/m_*$. The modification of the above for power-law distributions of stars (or brown dwarfs) of various masses is straightforward. We examine six cases:

1. Red stars taken to be M8 stars with $M_* = 0.2\ M_\odot$, $\log L_* = -2.2$, $T_{\rm eff} = 2400$ K.
2. Red stars just above the hydrogen-burning mass limit with $M_* = 0.08\ M_\odot$, $\log L_* = -3.8$, $T_{\rm eff} = 1525$ K.
3. Old (10^{10} yr) brown dwarf stars with $M_* = 0.07\ M_\odot$, $\log L_* = -5.25$, $T_{\rm eff} = 880$ K (Stevenson 1991; Burrows et al. 1997).
4. A mixed red star, brown dwarf model with a continuous power-law distribution with $\alpha = -1$, where $dN(m)/dM \propto m^{-\alpha}$ extending from 0.2 to 0.02 $M_\odot$.
5. A brown dwarf–only model with $\alpha = -1$ and extending from 0.07 to 0.02 $M_\odot$.
6. A white dwarf model with $M = 0.7\ M_\odot$, $\log L_* = -2.5\ L_\odot$, and $T = 8000$ K. This model is included since white dwarfs are a favored constituent of the Milky Way halo (Alcock et al. 1997a; 1997b; Graff et al. 1998).

To evaluate the emission from a stellar or brown dwarf halo we need estimates of the halo mass, $M_{\rm halo}$, the core radius, and the maximum extent. Ashman (1992) quotes an empirical relation between the core radius and the luminosity of the galaxy derived by Kormendy (1990) $R_{\rm core} = 5.9(L_B/10^9\ L_\odot)^{0.34}$ kpc. Taking $L_B = 3.7 \times 10^{10}\ L_\odot$ (e.g., Rupen 1991) gives $R_{\rm core} \sim 18$ kpc. From H I (Rupen 1991) we find $V_{\rm max} = 275$ km s^{-1}. With the arbitrary assumption of $R_{\rm max} = 30$ kpc and application of equations (1) and (2), we derive a total halo mass of $3.5 \times 10^{11}\ M_\odot$. It should be emphasized that these estimates are highly uncertain because of the effects of high inclination, internal reddening, and model uncertainties; we use these values only as representatives of a broad range of halo properties.

The variation of brightness can be derived using equations (3) and (4) for the various models (Table 4). Figure 7 shows the results of the model calculations along with the *ISO* observational limits at 12, 20, 30, and 50 kpc. Also included is the surface brightness observed along the minor axis in the visible (Näslund & Jörsäter 1997) but extrapolated to 4.5 μm using the colors of an M8 star ($V - M \sim 7.5$ mag). Thus, while the visible light observations constrain spectral types earlier than M8 better than these *ISO* measurements, the *ISO* data constrain the numbers of very red objects, i.e., very late M stars and brown dwarfs.

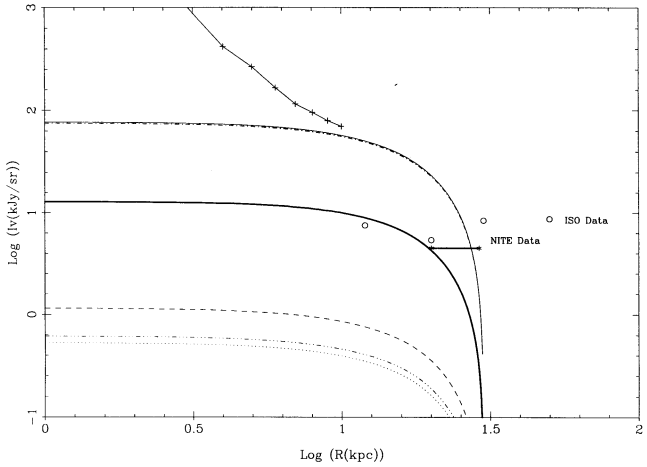

FIG. 7.—A number of models for the 4.5 μm emission from the halo of NGC 4565 are compared with the observations. The 3 σ *ISO* upper limits are shown as circles. The 3 σ upper limit at a comparable radius from the NITE rocket experiment is shown as a solid bar (Uemizu et al. 1998). *Top to bottom*: 0.2 $M_\odot$ stars (*solid line*) and almost on top of this curve a 0.02–0.2 $M_\odot$ distribution (*dash-dotted line*); 0.08 $M_\odot$ stars at the hydrogen-burning mass limit (*thick solid line*); 0.07 $M_\odot$ brown dwarfs (*dashed line*); white dwarfs (*dash-dot-dotted line*); 0.02–0.07 $M_\odot$ brown dwarfs (*dotted line*). The plus signs connected by a solid line denote the visible light data from Näslund & Jörsäter (1997) extrapolated to the 4.5 μm radiation expected from a halo of M8 stars.

All these constraints must be taken with a grain of salt. After all, there are fundamental difficulties in setting limits on a halo of unknown geometry composed of objects whose luminosity, age, metallicity, and subsequent emission are also unknown. Figure 8 gives a measure of the uncertainty in these results due to the unknown geometry of the putative halo. Model 2, consisting of 0.08 $M_\odot$ stars, was evaluated for five different values of the core radius (5, 8, 10, 15, and 20 kpc) compared with the nominal value of 18 kpc used for all other calculations. The resultant spread of values is less than a factor of 2 for the most reasonable range of core radii (10–20 kpc). Other geometrical factors, such as flattening of the halo and maximum extent, will have comparable effects on the predicted brightness of the halo.

The model consisting of 0.08 $M_\odot$ objects, just above the hydrogen-burning limit, is just barely ruled out by the observations. Because of the uncertainties in the model (unknown core radius, deviations from blackbody emission,

TABLE 4

MODELS FOR NGC 4565 HALO

Model	Mass ($M_\odot$)	α	N_* (10^{12})	$\langle M_* \rangle$ ($M_\odot$)	$L_{\rm halo}$ ($10^9\ L_\odot$)	F_* (Jy)	I_ν(12 kpc) (kJy sr^{-1})	I_ν(20 kpc) (kJy sr^{-1})
1.....	0.2	...	1.8	0.2	9	0.72	51	23
2.....	0.08	...	4.3	0.08	0.76	0.15	8.9	4.2
3.....	0.07	...	5.0	0.07	0.03	0.01	0.8	0.4
4.....	0.02–0.2	1.0	2.6	0.13	7	0.70	49	23
5.....	0.02–0.07	1.0	7.0	0.05	0.015	0.005	0.34	0.16
6.....	0.7	...	0.5	0.7	1.5	0.006	0.41	0.18

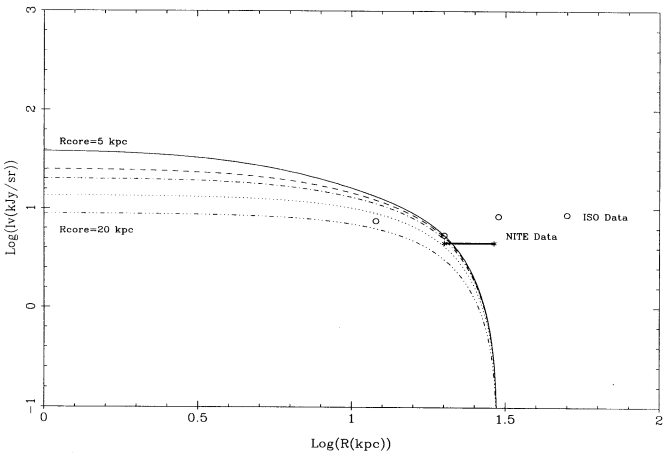

FIG. 8.—Model for the 4.5 μm emission from the halo of NGC 4565 as a function of core radius. The model takes the parameters of model 2 (0.08 $M_\odot$ stars) but for core radii of 5, 8, 10, 15, and 20 kpc. The 3 σ *ISO* upper limits are shown as circles. The 3 σ upper limit at a comparable radius from the NITE rocket experiment is shown as a solid bar (Uemizu et al. 1998).

other geometrical effects in the halo such as flattening, etc.) we cannot state unequivocally that hydrogen-burning stars of any mass are inconsistent with the *ISO* observations. However, the constraints on red dwarf stars in a spherical halo are strong, and only models invoking a narrow distribution of stars near the hydrogen mass limit can be considered as consistent with the *ISO* limits described herein. The M8 star model 1 with a mass-to-luminosity ratio (M/L) of about 40 in solar units at 4.5 μm is ruled out by these observations, but model 2 with 0.08 $M_\odot$ stars has $M/L \sim 450\, M_\odot/L_\odot$ and would be barely consistent with the data.

Halo populations consisting solely of brown dwarfs or white dwarfs are not constrained by these observations. New models for white dwarf stars (Saumon & Jacobsen 1999) are even bluer than the model used here, so that the *ISO* limits on this population are probably even weaker than Figure 7 indicates.

Both the *ISO* and extrapolated visible light observations rule out the presence of a stellar halo consisting of a broad range of red main-sequence stars. Gilmore & Unavane (1998) have measured a number of other edge-on spirals with similar negative results. The *ISO* data constrain models consisting of the reddest main-sequence dwarfs but are not sensitive enough to constrain models consisting only of the brown (or white) dwarfs. The conclusion that red stars do not form the halo is also consistent with ground-based near-IR observations toward NGC 100 (Casali & James 1995) and with *Hubble Space Telescope* observations of the halo of the Milky Way (Flynn et al. 1996). While numerous dynamical models (Chabrier, Segretain, & Mera 1996; Alcock et al. 1997b; Gyuk, Evans, & Gates 1998) argue against brown dwarfs making up the major part of galaxy halos, more sensitive observations with SIRTF will be needed to determine definitively whether substellar objects, isolated or in clusters (Kerins 1998), play any role in forming halos of galaxies.

The ISOCAM data presented in this paper were analyzed using CIA, a joint development by the ESA Astrophysics Division and the ISOCAM Consortium. C. A. B. would like to acknowledge the hospitality of Jean-Loup Puget and the Institut d'Astrophysique Spatiale (Orsay, France) and of the Dominion Radio Astrophysical Observatory (Penticton, Canada). This work was funded by an *ISO* data analysis grant from NASA. IPAC is operated for NASA by JPL and the California Institute of Technology under a contract with Caltech. The NASA Extragalactic Database was particularly valuable in the selection of NGC 4565. An anonymous referee provided useful comments that significantly improved the presentation of these results.

REFERENCES

Ashman, K. M. 1992, PASP, 104, 1109
Alcock, C., et al. 1993, Nature, 365, 621
———. 1997a, ApJ, 479, 119
———. 1997b, ApJ, 486, 697
Aubourg, E., et al. 1993, Nature, 365, 623
Bahcall, J. N., & Soneira, R. M. 1980, ApJS, 44, 73
Bernard, J-P., Boulanger, F., Desert, F. X., Girard, M., Helou, G., & Puget, J.-L. 1994, A&A, 291, L5
Burrows, A., et al. 1997, ApJ, 491, 856
Casali, M. M., & James, P. A. 1995, MNRAS, 274, 709
Casertano, S., & Van Gorkom, J. 1991, AJ, 101, 1231
Chabrier, G., & Baraffe, I. 1997, A&A, 327, 1039
Chabrier, G., Segretain, L., & Mera, D. 1996, A&A, 468, 21
Flynn, C., Gould, A., & Bahcall, J. N. 1996, ApJ, 466, L55
Geballe, T. R., et al. 1996, ApJ, 467, L101
Gilmore, G., & Unavane, M. 1998, MNRAS, 301, 813
Good, J. 1994, in The Explanatory Supplement to the *IRAS* Infrared Sky Survey Atlas, ed. S. Wheelock (JPL Publication 94-11) (Pasadena: JPL)
Graff, D. S., Laughlin, G., & Freese, K. 1998, ApJ, 499, 7
Gyuk, G., Evans, N. W., & Gates, E. I. 1998, ApJ, 502, 29
Kent, S. M. 1986, AJ, 91,1301
Kormendy, J. 1990, in Evolution of the Universe of Galaxies, ed. R. G. Kron (Provo, UT: BYU Press), 109
Kerins, E. J. 1998, A&A, 328, 5
Leggett, S. K., Allard, F., & Hauschildt, P. H. 1998, ApJ, 509, 836
Lequeux, J., Combes, F., Dantel-fort, M., Cuillandre, J.-C., Fort, B., & Mellier, Y. 1998, A&A, 334, L9
Lequeux, J., Fort, B., Dantel-fort, M., Cuillandre, J.-C., & Mellier, Y. 1996, A&A, 312, L1
Marley, M. S., et al. 1997, Science, 272, 1919
Näslund, M., & Jörsäter, S. 1997, A&A, 325, 915
Rand, R. J., Kulkarni, S. R., & Hester, J. J. 1992, ApJ, 396, 97
Reach, W. T., et al. 1995, Nature, 374, 521
Rice, W., Merrill, K. M., Gatley, I., & Gillett, F. C. 1996, AJ, 112, 114
Rudy, R. J., Woodward, C. E., Hodge, T., Fairfield, S. W., & Harker, D. E. 1997, Nature, 387, 159
Rupen, M. P. 1991, AJ, 102, 48
Sackett, P. D., Morrison, H. L., Harding, P., & Boroson, T. A. 1994, Nature, 370, 441
Saumon, D., Bergeron, P., Lunine, J., Hubbard, W. B., & Burows, A. 1994, ApJ, 424, 333
Saumon, D., & Jacobsen, S. B. 1999, ApJ, 511, L107
Simard, L., & Pritchett, C. 1994, AJ, 107, 503
Starck, J. L., et al. 1998, A&A, submitted
Stevenson, D. J. 1991, ARA&A, 29, 163
Trimble, V. 1987, ARA&A, 25, 425
Uemizu, K., Bock, J. J., Kawada, M., Lange, A. E., Matsumoto, T., Watabe, T., & Yost, S. A. 1998, ApJ, 506, L15
Vogler, A., Pitesch, W., & Kahabka, P. 1996, A&A, 305, 74